IAEA nuclear fusion

PAPER • OPEN ACCESS

Non-disruptive error field measurement in DIII-D low safety factor plasmas and projection to ITER

To cite this article: Q.M. Hu *et al* 2025 *Nucl. Fusion* **65** 016006

OPEN ACCESS
IOP Publishing | International Atomic Energy Agency

Nuclear Fusion

Nucl. Fusion **65** (2025) 016006 (12pp)

https://doi.org/10.1088/1741-4326/ad8def

Non-disruptive error field measurement in DIII-D low safety factor plasmas and projection to ITER

Q.M. Hu[1,*], N.C. Logan[2], C. Paz-Soldan[2], J. Barr[3], S.K. Kim[1], J. Hanson[2], Y.Z. Jiang[3], S.M. Yang[1], A. Bortolon[1], W. Choi[3], Y.Q. Liu[3], J.-K. Park[4], E.J. Strait[3] and Q. Yu[5]

[1] Princeton Plasma Physics Laboratory, Princeton, NJ 08543-0451, United States of America
[2] Columbia University, New York, NY 10027-6900, United States of America
[3] General Atomics, PO Box 85608, San Diego, CA 92186-5608, United States of America
[4] Seoul National University, Seoul, Korea, Republic Of
[5] Max-Planck-Institut für Plasmaphysik, 85748 Garching, Germany

E-mail: qhu@pppl.gov

Received 17 May 2024, revised 15 October 2024
Accepted for publication 1 November 2024
Published 13 November 2024

Abstract

Previous experiments in DIII-D (Paz-Soldan *et al* 2022 *Nucl. Fusion* **62** 126007) introduced a method to identify intrinsic error fields (EFs) in tokamaks with minimal disruption risk by promptly healing driven magnetic islands during the conventional 'compass scan'. This paper presents recent experimental and numerical advancements in extending this approach to low q_{95} plasmas, and projects its applicability to ITER. Non-disruptive EF measurement is achieved at $q_{95} = 4.5$ and 3.9 without any initial EF correction (EFC) by reducing the time between the occurrence of the locked mode (LM) and control action to 10 ms and increasing the density 50%–100%. However, 50% correction of the intrinsic EF is required to achieve island healing at $q_{95} = 3.2$ with 10 ms delay for the control action. Nonlinear two-fluid modeling with the TM1 code reproduces the DIII-D experimental observations, indicating that promptly turning off the 3D coil current reduces both magnetic island width and electromagnetic force, while raising the density increases plasma viscosity, facilitating magnetic island healing. The simulations show that for scenarios with $q_{95} = 3.2$, lowering the control action time to 5 ms will lead to island healing without EFC. TM1 simulations are extended to future ITER scenarios with 5 MA and 7.5 MA plasma currents, predicting the dependence of required density rise on action time and EF amplitude. These simulations indicate that, benefiting from the much longer resistive time, island healing can be successfully achieved in ITER when taking control action 100–500 ms after a LM occurrence.

Keywords: error field measurement, disruption, ITER

(Some figures may appear in colour only in the online journal)

* Author to whom any correspondence should be addressed.

1. Introduction

Intrinsic error fields (EFs), arising from imperfections in magnetic field-coil manufacture and assembly, have been a concern in tokamaks since the 1970s [1–7]. These EFs, often with magnitudes as small as one part in 10^4 of the toroidal field, can detrimentally affect plasma rotation, confinement, and even trigger disruptions by inducing locked magnetic islands [8–13]. To mitigate these effects, tokamaks are equipped with EF correction coils (EFCCs) [3], designed to trim the non-axisymmetric field and counteract the intrinsic errors, particularly that driving magnetic island at the $m/n = 2/1$ (where m and n are the poloidal and toroidal mode number) rational surface. The key element for the correction of intrinsic EFs is its measurement, which informs the current waveform (including amplitude and phase) for the EFCCs in the experiment operation.

In recent decades, various plasma-based techniques have emerged for empirically measuring the intrinsic EFs, including: (1) the 'compass scan', which involves ramping up EFCC current to induce magnetic islands at different toroidal phases, allowing derivation of EF amplitude and phase. Widely adopted in tokamaks worldwide, this method is a staple in EF measurement [2, 8, 10, 11, 14–19]. (2) Electromagnetic (EM) torque balance on a saturated island [20–22], which interacts the magnetic island using low-frequency EFCC current, revealing the intrinsic EF information through the island dynamic. (3) Plasma response-based optimization [15, 23–26], which assesses rotation braking by adjusting EFCC current to achieve maximal angular momentum. While robust, these methods face challenges in early tokamak operation, especially for ITER, due to the need for either producing disruptive island and or precise plasma diagnostics. Developing a non-disruptive EF identification strategy, requiring minimal diagnostics and actuators while remaining reliable for low q_{95} values down to 3, is thus imperative.

Recent DIII-D experiments [27] have demonstrated an improved compass scan approach for non-disruptive EF measurement, utilizing only magnetic diagnostics and asynchronous control of the EFCCs along with a density actuator (gas or pellets). This method employs prompt healing of the magnetic island to minimize the disruption risk, achieved by swiftly turning off EFCC current to eliminate the drive for the locked magnetic island, and concurrently increasing density via gas puffing to stabilize it. These actions, integrated into the plasma control system (PCS), are activated promptly upon detection of the magnetic island. Furthermore, successful replication of this technique in MAST-U and JET [28] confirms its robust applicability across different devices. However, extrapolating this method to ITER necessitates addressing several challenges outlined in [27], including (1) operating at lower edge safety factor ($q_{95} \sim 4.5$ compared to ITER's $q_{95} \sim 3.0$), (2) EF correction (EFC) was performed in the demonstration experiment, but the inability to fully correct the intrinsic EF during early tokamak operation, and (3) potential differences in the growth timescale of locked magnetic islands in ITER compared to recent devices. Addressing these challenges requires further experiments on existing recent devices to inform the first two questions, while nonlinear modeling, validated by recent experiments, can aid in resolving the third question.

In this work, experiments are performed in the DIII-D tokamak to extend the non-disruptive EF measurement method to q_{95} as low as 3.2. The investigation examines the sensitivity to varying degrees of EFC and the timing of actions to deactivate EFCC current and initiate gas puffing upon island detection across different q_{95} values. The experimental results indicate the method's viability without EFC for $q_{95} = 4.5$ and 3.9, with corresponding action times of 200 ms and 10 ms, respectively. However, for $q_{95} = 3.2$, effectiveness is observed only with 50% EFC and 10 ms action time. Nonlinear MHD simulations conducted using the TM1 code [29–31] offer insights into experimental observations, demonstrating that promptly deactivating EFCC current diminishes island drive and EM force, while increased density enhances plasma viscosity, facilitating magnetic island healing. By using the experimental equilibrium and profiles, the modeling consistently simulate the required density for island healing. The simulations predict that reducing the control action time to 5 ms could achieve island healing without EFC for $q_{95} = 3.2$. Based on these consistencies with DIII-D experiments, the TM1 simulations are extended to ITER 5 MA and 7.5 MA plasmas to project the feasibility of this method. Simulations project successful island healing with control action taken 100–500 ms post-LM penetration and density increased by 100%. The organization of this paper is as follows: section 2.1 introduces the experimental setup, and section 2.2 presents the experimental results. Section 3 presents the nonlinear modeling for the DIII-D experiment. The predictions of this method for ITER 5 MA and 7.5 MA plasmas are introduced in section 4. Finally, section 5 contains concluding remarks and a summary of key findings.

2. Experimental results

2.1. Experimental setup

The DIII-D experiments detailed in this study extend the non-disruptive EF measurement method to q_{95} values as low as 3.2, building upon the discharge initiated in [27]. The DIII-D Ohmic discharges presented here are configured in an upper single null configuration as shown by the poloidal cross section of plasma shape in figure 1(a), with major and minor radii of $R = 1.7$ and $a = 0.6$ m, respectively. The plasma current is held constant at 0.8 MA, while the toroidal field is systematically adjusted from $B_t = 1.4$ T to 1.0 T, resulting in decreasing q_{95} values from 4.5 to 3.2. Figures 1(b)–(d) shows the profiles of safety factor q, electron density and temperature measured by Thomson Scattering [32] for the Ohmic plasmas, with a core line-averaged density of 1.5×10^{19} m^{-3} prior to the compass scan. The 2/1 rational surface shifts from $\psi_N = 0.69$ to 0.8 as q_{95} deceases from 4.5 to 3.2. The in-vessel coils [33], consist of a lower row (IL) and an upper row (IU) as shown in figure 1(a), are configured to generate $n = 1$ non-axisymmetric magnetic perturbations for both EFC and compass scan procedures. The toroidal phase difference $\Delta\Phi_{UL} = 240°$ between the IU and IL coil currents is used to

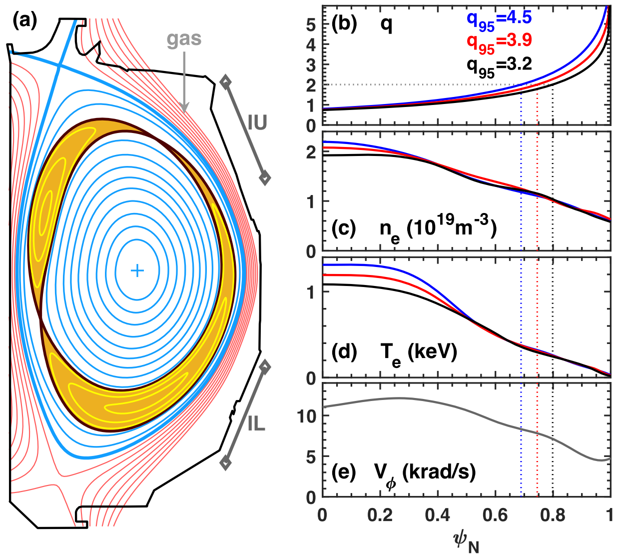

Figure 1. Equilibrium and profiles of target plasma in terms of (*a*) poloidal cross-sections of plasma shape and the 2/1 magnetic island for $q_{95} = 3.2$, profiles of (*b*) safety factor q, (*c*) electron density and (*d*) temperature for $q_{95} = 4.5$, 3.9 and 3.2, and (*e*) the plasma toroidal rotation. Here, the I-coils (IL, IU) and Gas puffing location are shown in (*a*), and the dotted lines in (*b*)–(*e*) indicate the $m/n = 2/1$ rational surface.

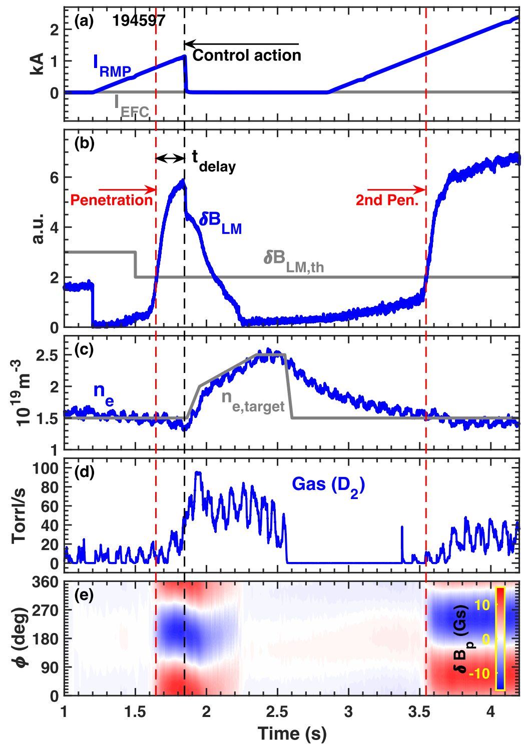

Figure 2. Time history of shot 194597 showing successful island healing with density increase and without EFC. (*a*) I-coil current for EFC and RMP, (*b*) LM signal and threshold for detecting it in PCS, (*c*) line-averaged density and feedforward target density, (*d*) gas puffing rate, and (*e*) time evolution of the poloidal magnetic perturbation in the toroidal array showing the onset and healing of LM.

achieve optimal resonant coupling with the plasma. The LM signal, monitored by saddle loop coils, is integrated into the PCS to enable real-time LM detection. In addition, the core line-averaged electron density, measured via interferometer [34], is fed into the PCS for the feedback control of density rise through adjustments to the gas puffing rate. The location of D_2 gas puffing is shown in figure 1(*a*).

Figure 2 illustrates the temporal evolution of shot 194597, showcasing the key elements of the non-disruptive EF measurement process. Shot 194597 is a reproduction of shot 178328 from [27], with $q_{95} = 4.5$, except for the deactivation of EFC, denoted by $I_{EFC} = 0$ in figure 2(*a*). In DIII-D, the initial guess of EFC is from an empirical PCS algorithm [17], and the required I-coil current for EFC is approximately 0.9 kA at $-55°$ as illustrated in figure 7. For clarity, the I-coil current is segmented into two components: one dedicated to EFC and the other for generating resonant magnetic perturbation (RMP) used in the compass scan, though the applied spectrum of both components is the same. The fundamental concept underlying the non-disruptive EF compass scan entails the following steps: (1) upon surpassing a threshold, the linearly increasing RMP current (I_{RMP} in figure 2(*a*)) initiates the first LM penetration, evident from the rapid rise in the LM signal δB_{LM} depicted in figure 2(*b*). (2) The PCS automatically identifies LM occurrence when its amplitude (δB_{LM}) surpasses the default threshold ($\delta B_{LM,th}$). (3) Following a time delay (t_{delay}) post-LM detection ($t_{delay} = 200$ ms in this case), the PCS undertakes actions to avoid LM: it promptly ceases the RMP current to eliminate the LM drive (as depicted in figure 2(*a*)), while concurrently activating gas puffing to elevate density in accordance with the feedforward target density (figure 2(*c*)). Here, the delay time $t_{delay} > 0$ is necessary to avoid the uncertainty in detecting the LM onset via magnetic diagnostics. The augmented density stabilizes the LM, resulting in a ∼50% density rise at $t = 2.25$ s, accompanied by complete island healing. This intervention effectively avoids the LM island, evident from the δB_{LM} evolution (figure 2(*b*)) and poloidal magnetic perturbation δB_p (figure 2(*d*)). Following island healing and plasma recovery, the process is iterated for a second compass scan. Notably, the LM undergoes a slight phase shift and locks to the EF upon RMP current cessation, as illustrated in the 2D contour plot of the LM poloidal magnetic perturbation (figure 2(*e*)).

Figure 2 clearly demonstrates the suitability of this method for early tokamak operation, as it relies solely on basic diagnostics and actuators, encompassing magnetic and density measurements, as well as gas puffing or pellets. To underscore its robustness for ITER-relevant q_{95} values (≈3.2), we extend this method to lower q_{95} values in the subsequent subsection. Through comprehensive scanning of parameters such as delay time (t_{delay}), magnitude of density rise, and EFC fraction, non-disruptive EF compass scans are extended to $q_{95} = 3.2$.

2.2. Non-disruptive EF measurement at lower q_{95}

Challenges escalate when extending this method to lower q_{95} plasmas due to faster growth and larger ultimate width of

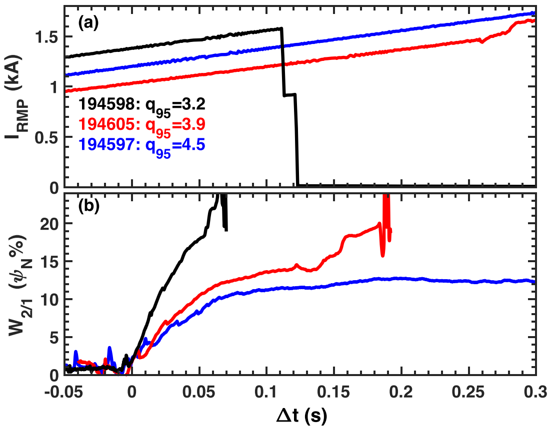

Figure 3. The 2/1 LM island grows faster and larger at lower q_{95}. Time evolution of (*a*) RMP current for compass scan, and (*b*) the derived 2/1 magnetic island width for $q_{95} = 4.5$ (blue), 3.9 (red) and 3.2 (black). Here, the data of shot 194598 and 194605 are from the second compass scan, $\Delta t = 0$ corresponds to the time of LM occurrence.

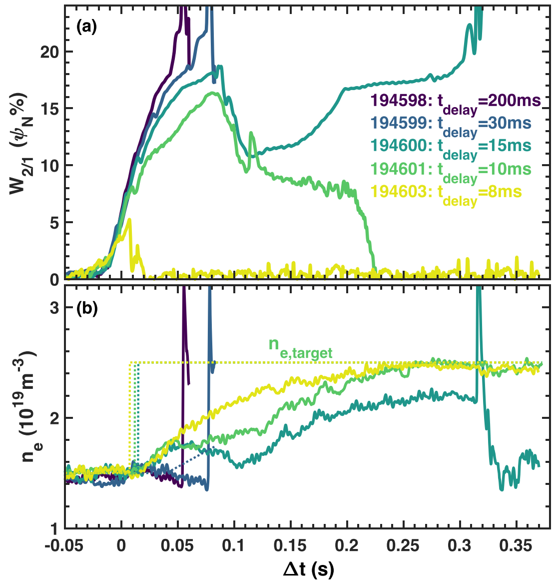

Figure 4. The island healing is sensitive to the delay time at low q_{95}. Time history of the (*a*) 2/1 LM island width, and (*b*) line-averaged density for $q_{95} = 3.2$ with t_{delay} varied from 200 ms to 8 ms. Here, the dotted curves in (*b*) indicate the target density.

the 2/1 LM island. Figure 3 illustrates the temporal evolution of the RMP current alongside the derived $m/n = 2/1$ LM island width for discharges across various q_{95} values. Here, the island width is derived from measured radial magnetic perturbations and the equilibrium using the formula $W = 4(L_s r_s \delta B_r / m B_t)^{0.5}$ [9], where $L_s = Rq^2/r_s q'$ represents the magnetic shear length, r_s denotes the minor radius of the 2/1 rational surface, $q' = \mathrm{d}q/\mathrm{d}r$, and δB_r and B_t corresponds to measured radial magnetic perturbation and equilibrium toroidal field, respectively. Subsequently, the derived magnetic island width is normalized to the normalized poloidal flux ψ_N. For shot 194597 with $q_{95} = 4.5$, the 2/1 magnetic island width (referred to as $W_{2/1}$) grows and saturates at 12% of the normalized poloidal flux within ≈70 ms. Remarkably, even without control intervention, it does not culminate in a major disruption [1], as evidenced by the second compass scan in figure 2. Conversely, for shot 194605 with $q_{95} = 3.9$, $W_{2/1}$ grows to $0.15\psi_N$ in ≈60 ms, subsequently leads to major disruption. Moreover, in shot 194598 with $q_{95} = 3.2$, $W_{2/1}$ grows even faster and larger, reaching $0.2\psi_N$ in around 50 ms. The accelerated growth of the 2/1 LM in shot 194598 causes plasma disruption much earlier than the initiation of control action with $t_{\mathrm{delay}} = 200$ ms. Notably, $W_{2/1}$ exhibits additional rapid expansion post-saturation but before disruption for $q_{95} = 3.9$ and 3.2, likely attributed to the emergence of additional LMs via mode coupling [35, 36].

It is crucial to initiate the control action as early as possible for effective island healing, as depicted in figure 4. The delay time since LM occurrence is systematically varied from 200 ms to 8 ms for $q_{95} = 3.2$, with the fraction of EFC ranging from 100% to 75%, and its impact on island healing and density rise is illustrated in figure 4. Results demonstrate that when the delay time exceeds 10 ms, island healing becomes unattainable due to the substantial growth of the 2/1 LM island, leading to significant density pump-out [31, 37] and impeding density rise, as exemplified by shot 194600 in figure 4(*b*), despite the discharge sustaining for over 300 ms post-LM occurrence. Conversely, for $t_{\mathrm{delay}} \leqslant 10$ ms, island healing is successfully achieved, necessitating a 65% density rise in 194601 with $t_{\mathrm{delay}} = 10$ ms, and no obvious density rise in 194603 with $t_{\mathrm{delay}} = 8$ ms. The disparity in the time evolution of island width and density in figure 4 unveils the distinct roles of turning off RMP and density rise: (1) immediately turning off RMP removes the drive for the LM island growth, resulting in a smaller saturated island width. Notably, the primary cause of island healing in shot 194603 is this effect, as the density rise responds too slow to influence it. (2) Owing to the delayed transport time of gas puffing, the density rise commences stabilizing the LM 50–100 ms post- action, with a further ≈100 ms typically required for complete island healing, as evidenced by shot 194600.

The density rise required to heal the LM island is contingent upon the EF amplitude (or EFC fraction), as demonstrated in figure 5 for $q_{95} = 3.9$. In DIII-D, the default current and phase for EFC are implemented in the PCS based on previous systematic studies [17], with the EFC fraction being adjustable. In shot 194605 with 50% EFC, the control action is on with $t_{\mathrm{delay}} = 20$ ms and $n_{e,\mathrm{target}} = 2.5 \times 10^{19}$ m^{-3} upon LM detection. Promptly turning off the RMP current results in the slow rotation of the 2/1 LM, depicted in figure 5(*c*), with the ensuing density increase further hastening its rotation ($\Delta t = 0.15$–0.2 s). Ultimately, island healing is realized at $\Delta t = 0.21$ s when the density is augmented by 50%. Conversely, shot 194608, devoid of EFC, initiates the control action with $t_{\mathrm{delay}} = 10$ ms and $n_{e,\mathrm{target}} = 3 \times 10^{19}$ m^{-3}. The overall evolution of the island width is same as that of shot

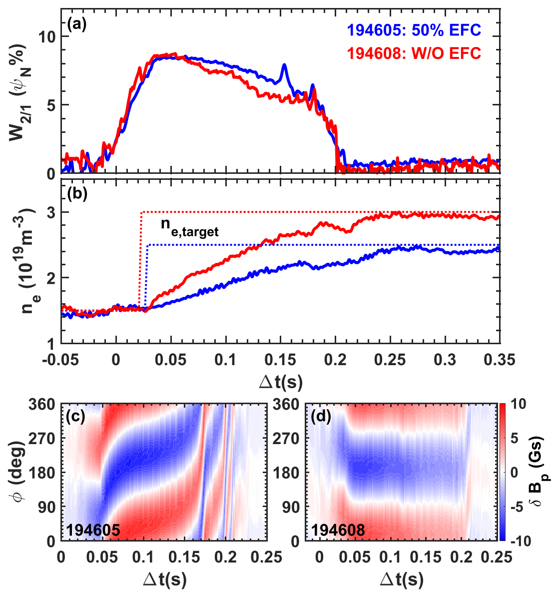

Figure 5. The required density rise depends on the fraction of EFC. Time history of the (*a*) 2/1 LM island width, and (*b*) line-averaged density and target density (dotted lines) for shot 194605 with 50% EFC and 194608 without EFC. 2D contour plot of the poloidal magnetic perturbation around island healing for (*c*) 194605 and (*d*) 194608. Here, $q_{95} = 3.9$, $t_{\text{delay}} = 20$ ms and $n_{\text{e,target}} = 2.5 \times 10^{19}$ m^{-3} for shot 194605, and $t_{\text{delay}} = 10$ ms and $n_{\text{e,target}} = 3 \times 10^{19}$ m^{-3} for shot 194608.

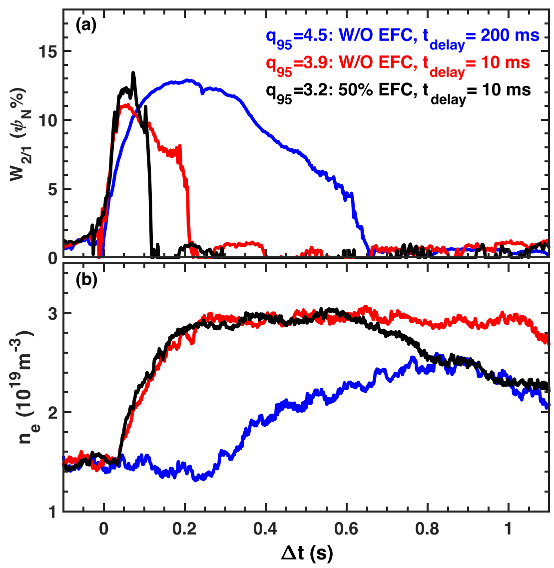

Figure 6. Island healing is achieved at different q_{95}. Time evolution of (*a*) 2/1 LM island width, and (*b*) line-averaged density for $q_{95} = 4.5$, 3.9 and 3.2.

194605, except the 2/1 LM shifts its toroidal phase slightly and locks to the EF without rotating until final vanishing as shown in figure 5(*d*). Complete island healing is accomplished at $\Delta t = 0.202$ s with the density increased by 72%. For comparison, to attain island healing at $q_{95} = 3.2$, a 65% density increase is required for 100% EFC, and 78% for 50% EFC.

Island healing is realized at the three distinct q_{95} values through the optimization of the delay time and density rise, elucidated in figure 6. Specifically, island healing is robust for $q_{95} = 4.5$ and 3.9 without EFC, necessitating a density rise of around 50%, with corresponding t_{delay} of 200 ms and 10 ms, respectively. For $q_{95} = 3.2$, island healing is attainable only with no less than 50% EFC, a delay time of approximately 10 ms, and a minimum 65% density rise. Building upon the insights from shot 194603 (depicted in figure 4), we anticipate that complete island healing can be achieved without EFC by decreasing t_{delay} to ∼5 ms with a >60% density rise, although experimental demonstration is pending. Subsequently, we substantiate this projection through nonlinear modeling.

Based on the aforementioned scans, the compass scan has been successfully completed for plasmas with different q_{95}, providing valuable insights into the amplitude and phase required to compensate the EF, as shown in figure 7. The I-coil current trajectory and RMP threshold current (marked by crosses), where LM penetration and magnetic island formation occur, are plotted on a polar graph of amplitude and phase. The starting points of the compass scan, indicated by solid circles, represent fraction of EFCs applied (ranging from 0% to 100%). The RMP threshold current is fitted to a circle on the polar plot (black circles) with an 8% uncertainty margin, while the grey circles represent a ±10% deviation from the fit. The centroids of these circles (denoted by black stars) represent the optimal I-coil current and phase required to correct the intrinsic EF, which are found to be 0.873 kA at 125° for $q_{95} = 4.5$ in figure 7(*a*), 0.803 kA at 122° for $q_{95} = 3.9$ in figure 7(*b*), and 0.635 kA at 114° for $q_{95} = 3.2$ (figure 7(*c*)).

The newly measured EF values are consistent with the default EFC settings for $q_{95} = 4.5$, as indicated by solid circles with 100% EFC. However, a small deviation is observed for $q_{95} = 3.9$ (figure 7(*b*)), and a more significant 25% difference is noted for $q_{95} = 3.2$ (figure 7(*c*)). These discrepancies are likely due to variations in the target plasma over the extended period of time [27]. Furthermore, discharges marked in blue, red, and magenta demonstrate the successful completion of two compass scan pulses within a single discharge, illustrating the potential to reduce the number of dedicated discharges required for a full scan. Notably, at the lower $q_{95} = 3.2$, the penetration threshold for the second compass scan is higher (as seen in discharges 194603 and 194609 in figure 7(*c*)), due to insufficient recovery of density after a larger gas puff. This suggests that a longer time delay is necessary before initiating the second compass scan when significant gas puffing is applied.

3. Non-linear modeling for DIII-D experiments

To understand the DIII-D experimental results outlined in section 2, we use the TM1 code [29, 30] to simulate the EF penetration and island healing in the DIII-D Ohmic plasma with $m/n = 2/1$ helical magnetic boundary conditions. TM1 is a nonlinear two-fluid MHD code with cylindrical geometry and circular cross-section. The details of the model are introduced in [31], including the equations, assumptions and limitations, its input and its output. Toroidicity and plasma-shaping effects on the EF/RMP are introduced through the

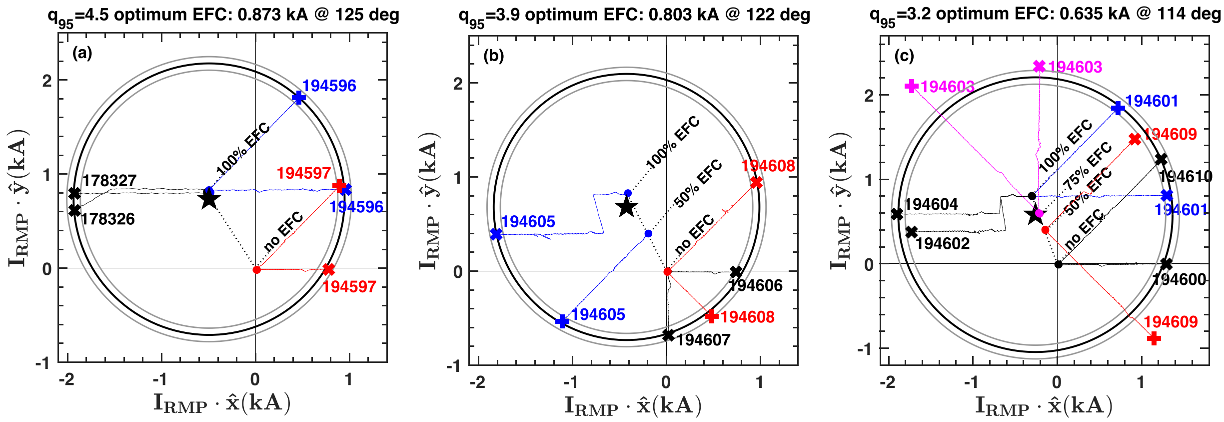

Figure 7. Compass scan results for EF measurement at (*a*) $q_{95} = 4.5$, (*b*) $q_{95} = 3.9$, and (*c*) $q_{95} = 3.2$. The black, blue, red and magenta solid circles are the start point with different fraction of EFC, and the trajectories of the I-coil current ends with the penetration threshold marked by '×' and '+'. Fitting of these penetration threshold in black circle reveals the optimum current and phase to correct EF as marked by '★'. Here, the '×' and '+' markers correspond to the first and second compass scan in a single discharge labeled in blue, red and magenta color. The fraction of EFC is also labeled for the solid circles.

use of the toroidal ideal MHD code GPEC [38], which computes the ideal MHD plasma response to the 3D vacuum field and decomposes the total magnetic perturbation into helical harmonics that serve as the boundary conditions for TM1. Previously,TM1 has been utilized to model the EF penetration in TEXTOR [39] and DIII-D [35, 40], as well as RMP-driven edge-localized mode (ELM) suppression in DIII-D and KSTAR [31, 37, 41–43].

In this section, we focus on the DIII-D plasmas with $q_{95} = 4.5$ and 3.2 as our simulation targets, and the equilibrium and profiles for the TM1 simulation and GPEC analysis are shown in figures 1(*b*)–(*e*). The plasma toroidal rotation in figure 1(*e*) is adopted from another experiment [44] with similar plasma parameters. The following transport coefficients calculated by the TRANSP code [45] are used $\mu = \chi_\perp = 3D_\perp = 1\ \mathrm{m}^2\ \mathrm{s}^{-1}$, here μ, $\chi_\perp$ and $D_\perp$ are the viscosity, thermal and particle diffusivity. To model the density rise, an additional time-dependent particle source is implemented in the electron continuity equation, with the assumption that density ramps to the target flattop within approximately 150 ms of the control action initiation (based on the behavior observed in shot 194608, as depicted in figure 5). The time evolution of the change in the density profile from the TM1 simulation, illustrated in figure 8, aligns with the density profile evolution characteristics observed with D_2 gas puffing, as indicated by the black dotted curves from shot 194597 at various time points.

TM1 simulations for shot 194597 with $q_{95} = 4.5$ are shown in figure 9. Ramps of the $n = 1$ RMP current at 40° are applied, a static intrinsic EF is also included in the simulations with 0.89 kA at −55° (equivalent to experiential measurement) to simulate shot 194597 without EFC. LM penetration occurs at $t = 0.37$ s when the RMP current exceeds the threshold, as illustrated in figure 9(*c*). The LM Island rapidly grows and saturates at 13% of the minor radius in ∼100 ms. Concurrent with the LM growth, it leads to density pump-out (depicted in figure 9(*b*)) and a rapid increase in EM force (shown in figure 9(*d*)), resulting in plasma rotation deceleration and

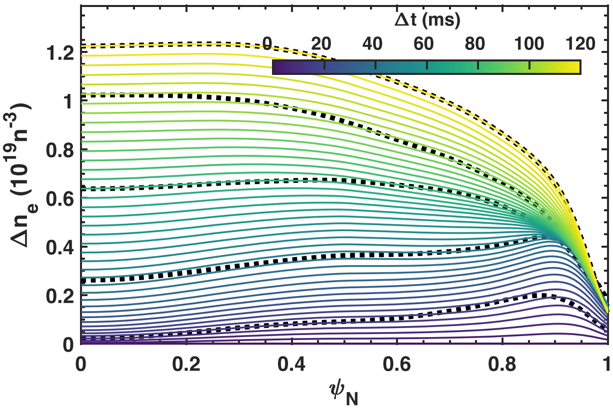

Figure 8. TM1 simulated change in the density profile since the control action is on. For comparison, the change in the density profile at different time from shot 194597 are shown in black dotted curves.

increased viscous force (as see in figure 9(*e*)). Here, the EM force $\boldsymbol{F}_{\mathrm{EM}} = \boldsymbol{j}_1 \times \boldsymbol{b}_{\mathrm{r}1}$, the viscous force $\boldsymbol{F}\mathrm{vs} = \rho\mu_\perp\nabla^2\boldsymbol{v}$, $\boldsymbol{j}_1$ and $\boldsymbol{b}_{\mathrm{r}1}$ represent the current density perturbation and magnetic perturbation [9, 46], respectively. At $t = 0.57$ s, 200 ms after LM occurrence, the control action is initiated. This action entails on the one hand, turning off the RMP current, which diminishes the drive for LM island, evident from the rapid drop in the island width. Concurrently, it reduces the EM force exerted on the magnetic island, as indicated by the decline in F_{EM} (figure 9(*d*)). On the other hand, the additional particle source is initiated with different target density rise (0%–100%) scanned in the simulations. As plasma density increases, plasma viscosity rises, leading to stabilizing effects on the LM island, as evidenced by the decreased island width (figure 9(*c*)). Island healing is achieved when the density rises by more than 45%, consistent with DIII-D experimental observations marked in figure 9(*b*). Additionally, faster density rise correlates with quicker island healing, due to the critical density being reached sooner.

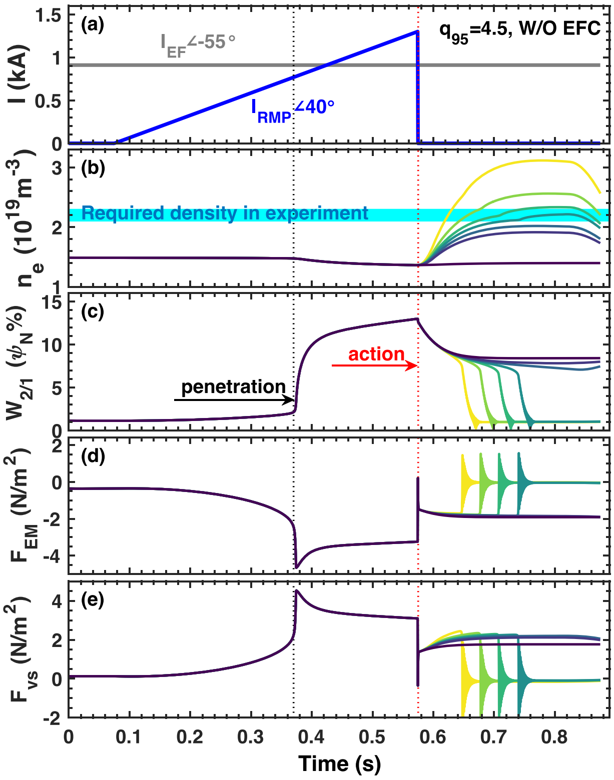

Figure 9. TM1 simulations for shot 194597 with $q_{95} = 4.5$, without EFC and different magnitude of density rise. Time history of (*a*) RMP and EF current, (*b*) line-averaged density, (*c*) 2/1 magnetic island width, (*d*) EM force, and (*e*) viscous force. Here, negative force means opposite to the direction of plasma rotation, and vice versa.

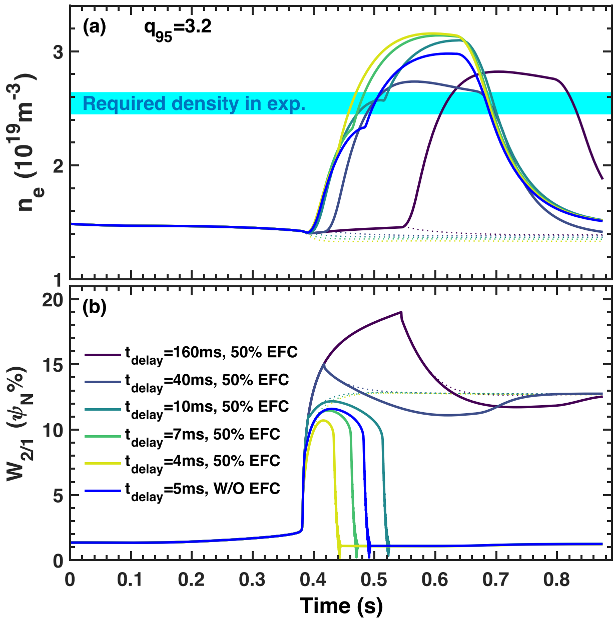

Figure 10. TM1 simulations for shot 194609 with $q_{95} = 3.2$, 50% EFC and different delay time. Time history of (*a*) line-averaged density, and (*b*) 2/1 magnetic island width. Here, t_{delay} is scanned from 160 ms to 4 ms, and an additional simulation without EFC and with $t_{\mathrm{delay}} = 5$ ms is shown in blue curve. The dotted curves show the simulations by turning off RMP at different t_{delay} but without density rise.

TM1 simulations for shot 194609 with $q_{95} = 3.2$ and 50% EFC are shown in figure 10. The setup for the EF and RMP current are same as figure 9 except the EF current is different. The LM penetration occurs at $t = 0.39$ s, and the island width grows rapidly and saturates at ∼20% of the minor radius if the control action is off. Then in the simulations, the control action is turned on with t_{delay} scanned from 160 ms to 4 ms, and the target density is set to increase 110%. It is evident that island healing can only be achieved when t_{delay} is 10 ms or less, and quicker healing is observed with shorter t_{delay}. For $t_{\mathrm{delay}} = 10$ ms, at the time of complete island healing, the density is increased by 70%, consistent with the observations from shot 194609 shown in figure 6. Moreover, the simulations reveal that the required density rise is lower for shorter t_{delay}, aligning with observations from shot 194603 shown in figure 4. In cases where $t_{\mathrm{delay}} > 10$ ms, the large LM island leads to density pump-out, hindering the density from reaching the target during the flattop, in line with observations from figure 4. Simulations with the RMP turned off, but without density rise, are depicted in dotted curves from comparison, highlighting the stabilizing effect of density rise on LM healing. Besides, additional simulations are conducted for this low q_{95} plasma without EFC, as shown in the blue curve in figure 10. It predicts that island healing can be achieved at $q_{95} = 3.2$ without EFC when an earlier control action is taken, i.e. $t_{\mathrm{delay}} = 5$ ms.

4. Projection for ITER early operation

Given the robustness demonstrated non-disruptive EF measurement method across DIII-D [27], JET and MAST-U [28], and the consistency between DIII-D experiments and TM1 simulations, it merits consideration to apply this method for ITER's early operation. In this section, we expand the TM1 simulations to ITER to investigate the viability of this method for $n = 1$ EF measurement during the early operation with $I_{\mathrm{p}} = 5$ MA and $B_{\mathrm{t}} = 1.8$ T, and $I_{\mathrm{p}} = 7.5$ MA and $B_{\mathrm{t}} = 2.65$ T. Figure 11 shows the equilibrium and profiles utilized for the simulations with $q_{95} = 3.2$ for both plasmas. The toroidal rotation in figure 11(*e*) is predicted using ASTRA transport simulations [47]. Specifically, for the 5 MA plasma, the rotation profile is calculated assuming 20 MW of ECH and 10 MW of NBI power, with a Prandtl number (Pr) of 0.3 and a ratio of toroidal momentum to thermal confinement time ($\tau_\phi/\tau_{\mathrm{E}}$) of 1. For the 7.5 MA plasma, it assumes 20 MW of ECH and 33 MW of NBI power, with a Prandtl number of 0.3 and $\tau_\phi/\tau_{\mathrm{E}} = 1$. The plasma viscosity is then derived from the assumed momentum confinement time (0.87 s for the 5 MA plasma and 1.8 s for the 7.5 MA plasma), and the following relation for the anomalous transport coefficients are used $\mu = \chi_\perp = 3D_\perp$. Given the planned use of pellets injection

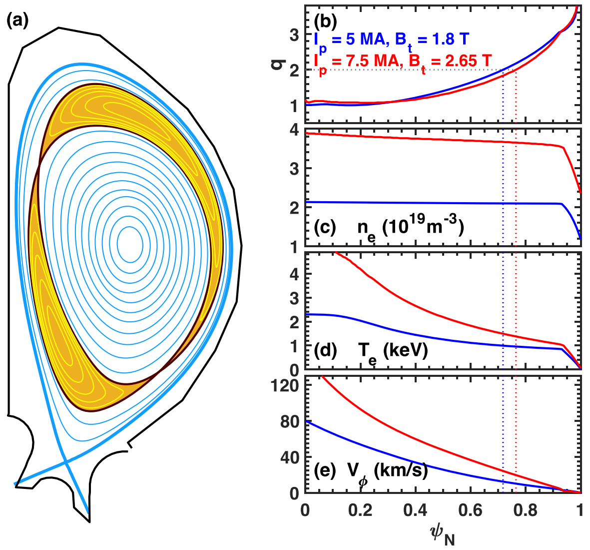

Figure 11. Equilibrium and profiles for the ITER $I_p = 5$ MA (blue) and 7.5 MA (red) plasmas in terms of (*a*) poloidal cross-sections of plasma shape and 2/1 LM island for $I_p = 7.5$ MA plasma, profiles of (*b*) safety factor q, (*c*) electron density, (*d*) electron temperature and (*e*) toroidal plasma rotation. Here, the dotted lines in (*b*)–(*e*) indicate the $m/n = 2/1$ rational surface.

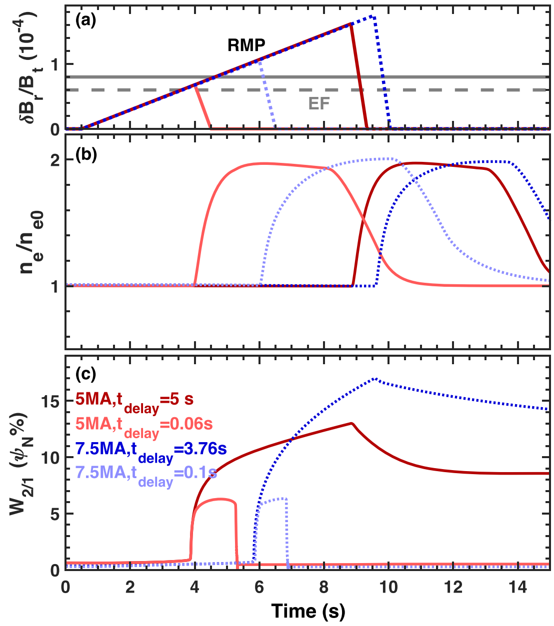

Figure 12. TM1 simulations for ITER 5 MA (solid curves) and 7.5 MA (dotted curves) plasmas with different t_{delay}. Time history of (*a*) RMP and EF amplitude δB_r normalized by B_t, (*b*) core line-averaged density normalized by the initial density, and (*c*) 2/1 magnetic island width.

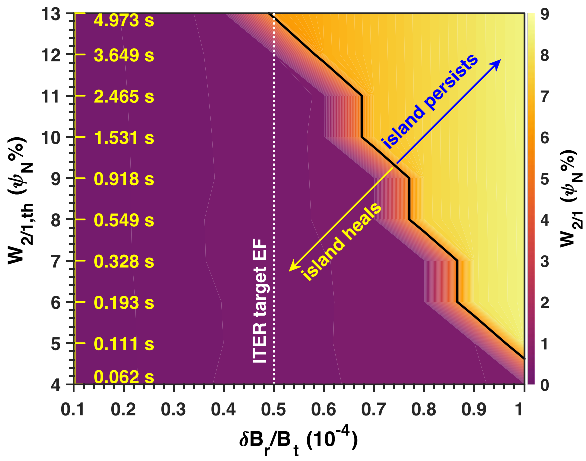

Figure 13. TM1 simulations results for ITER 5 MA plasma in terms of 2D contour plot of the 2/1 magnetic island width versus EF amplitude and t_{delay} (or 2/1 island width when the action is on). Here, the density rise is fixed with 100%, and the white vertical line shows the target EF amplitude in ITER.

as the primary gas fueling in ITER [48], the density response time is expected to be around 10 s ms due to its higher injection speed. For the ensuing simulation, it is assumed that the density rise will approximate the target flattop in 1.0 s.

Figure 12 illustrates the TM1 simulations for ITER plasmas with $I_p = 5$ and 7.5 MA. The RMP field follows a consistent ramping rate, with a subsequent 0.5 s ramp-down when the control action is initiated, as shown in figure 12(*a*). For $I_p = 5$ MA, an intrinsic EF amplitude of $\delta B_r/B_t = 0.8 \times 10^{-4}$ is applied, while for $I_p = 7.5$ MA, it is reduced to 0.6×10^{-4}. Compared to the initial value, the core line-averaged density is increased by 100% in 1 s as shown in figure 12(*b*). For $I_p = 5$ MA plasma, due to the much larger resistive time, the LM island takes more than 1 s to grow up and saturate after it opens at 3.9 s (dark red curve in figure 12(*c*)), one order longer than in DIII-D. This prolonged growth time allows for greater flexibility in timing the control action upon LM detection. Consequently, initiating the control action with $t_{delay} = 0.06$ s effectively heals the LM island, contrasting with $t_{delay} = 5$ s, where the island becomes too large for healing. Simulations for $I_p = 7.5$ MA plasma exhibit a similar trend, with the island requiring even more time to grow and saturate. Too late action has little effect on the island width.

The dependence of achieving full island healing on EF amplitude and t_{delay} is investigated through scanning for the $I_p = 5$ MA plasma with fixed 100% density rise. Specifically, the normalized EF amplitude $\delta B_r/B_t$ is scanned from 10^{-5} to 10^{-4}, while t_{delay} is varied from 0.062 s to 5 s. As depicted in the 2D contour plot of the saturated 2/1 magnetic island width after the control action versus $\delta B_r/B_t$ and t_{delay} in figure 13, it reveals that with $\delta B_r/B_t < 0.4 \times 10^{-4}$ and 100% density rise, island healing is consistently achieved cross $t_{delay} = 0.06$ s to 5 s. However, for $\delta B_r/B_t \geqslant 0.4 \times 10^{-4}$, the required t_{delay} decreases as the EF amplitude increases. Given the targeted EF amplitude of $\delta B_r/B_t \sim 0.5 \times 10^{-4}$ in ITER [4, 49], this non-disruptive EF measurement method appears robust for $t_{delay} < 4$ s.

A comprehensive scan is conducted, varying the density rise, EF amplitude, and the delay time, to predict the required density rise at different EF level and different t_{delay}. This prediction is illustrated in figure 14 for $I_p = 5$ MA and 7.5 MA. For $I_p = 5$ MA as shown in figure 14(*a*), it is evident that, for a fixed t_{delay} (i.e. 0.1 s), the required density rise increases from 5% to more than 100% as the EF amplitude increases

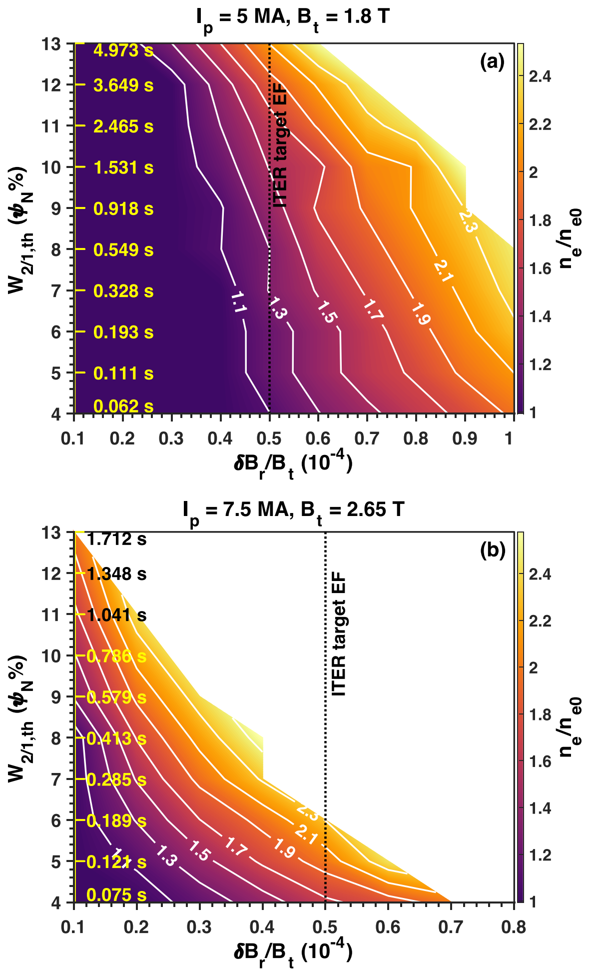

Figure 14. TM1 simulations for the required density rise to achieve island healing at different delay time and EF amplitude. 2D contour plot of required density rise versus $\delta B_r/B_t$ and t_{delay} for (*a*) $I_p = 5$ MA and (*b*) $I_p = 7.5$ MA.

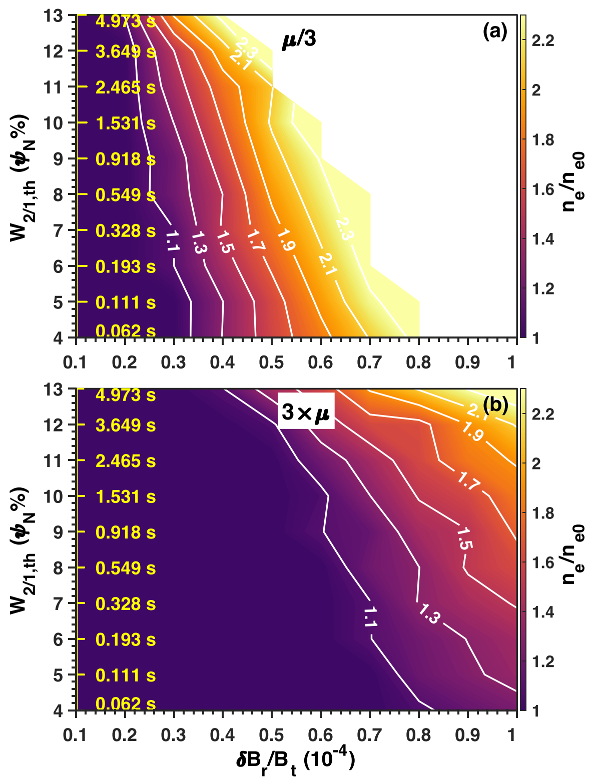

Figure 15. Sensitivity of TM1 simulations on plasma viscosity for the required density rise to achieve island healing at different delay time and EF amplitude at $I_p = 5$ MA. 2D contour plot of required density rise versus $\delta B_r/B_t$ and t_{delay} for (*a*) 1/3 and (*b*) 3 times of the plasma viscosity used in figure 14(*a*).

from 10^{-5} to 10^{-4}. Similarly, for a fixed EF amplitude, taking the ITER target EF for an example, the required density rise increases from 10% to more than 110% with t_{delay} increasing from 0.06 s to 5 s. For $t_{delay} < 0.6$ s, island healing is robust for the scanned EF range with 5%–130% density rise. Conversely, for $I_p = 7.5$ MA as shown in figure 14(*b*), while the overall trend is same as $I_p = 5$ MA, full island healing is more constrained with shorter t_{delay} or weaker intrinsic EF amplitude due to the larger magnetic island. For the target EF amplitude in ITER, the required density rise is more than 70% with $t_{delay} < 0.2$ s. Consequently, an earlier control action is imperative to prevent large island and disruption, particularly for the higher I_p plasma.

Given the important role of plasma viscosity in island healing, the nondisruptive EF measurement method is expected to be sensitive to the choice of plasma viscosity in the MHD simulations. The absence of a first-principles model for determining plasma viscosity in ITER introduces uncertainty into the extrapolation. To address this, additional simulations were performed to explore the sensitivity of the results to changes in plasma viscosity. In these simulations, the viscosity was varied to 1/3 and 3 times the value used in figure 14(*a*) for the $I_p = 5$ MA plasma, with the corresponding required density rise shown in figure 15. The results indicate that lower viscosity requires a larger density increase for island healing, and higher viscosity requires less. For example, with $\delta B_r/B_t = 0.5 \times 10^{-4}$ and $t_{delay} = 0.3$ s, the required density rise is 30% as shown in figure 14(*a*), but this increases to 70% for $\mu/3$ (figure 15(*a*)) and decreases to 10% for $3 \times \mu$ (figure 15(*b*)).

Finally, TM1 simulations are conducted to examine the influence of RMP ramp-down time on island healing. The simulations are performed for $I_p = 5$ MA with a 90% density rise and EF amplitude $\delta B_r/B_t = 0.8 \times 10^{-4}$, with the ramp-down time scanned from 0.5 s to 3 s as shown in figure 16(*a*). It shows robust island healing for 0.5–3 s ramp-down time, and faster RMP ramp-down leads to quicker island healing with less density rise as shown in figure 16(*b*). It has been assessed for ITER that turning off its EFCC current from the engineering limit current to zero will take about 3 s for the top and bottom rows, and less than 1 s for the middle row [28, 50].

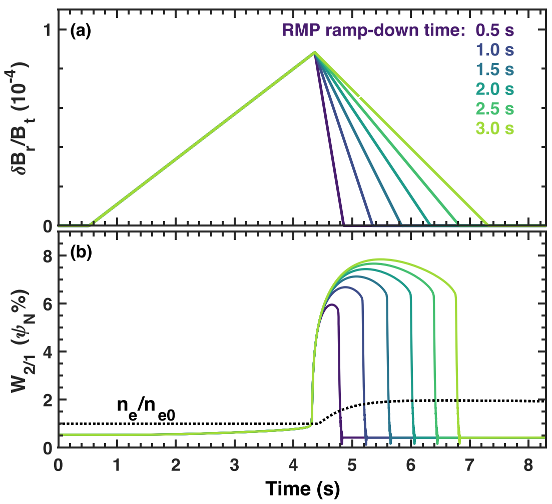

Figure 16. TM1 simulations results for the influence of RMP ramp-down time on island healing in ITER 5 MA plasma with 90% density rise and $\delta B_r/B_t = 0.8 \times 10^{-4}$. Time evolution of (*a*) RMP waveform with ramp-down time varying from 0.5 s to 3 s, and (*b*) the 2/1 magnetic island width. The dotted curve in (*b*) shows the normalized core line-averaged density.

Additionally, there is consideration for utilizing the ELM control coils for $n = 1$ EFC in ITER, given their ability to be turned off much faster, in less than 0.5 s. Consequently, we conclude that the non-disruptive EF compass scan method is robust for ITER's early operation.

5. Discussion and summary

The DIII-D experiments and nonlinear modeling presented in this work have demonstrated the robustness of non-disruptive EF measurement with ITER relevant low q_{95}. Despite these promising results, several open questions persist regarding the ultimate deployment of such a technique to a fusion-grade tokamak plasma:

(1) Full island healing without EFC has not been achieved for $q_{95} = 3.2$, although the nonlinear simulations suggest the possibility by reducing the delay time since LM occurrence. Future experimental demonstrations are warranted to validate this potential.
(2) The present DIII-D experiments are conducted in low current plasma. Analytical theories [51, 52] have indicated that the dynamics of LM penetration depend on the ion Larmor radius ρ^* through the linear layer physics. For matched q_{95} and β_N, increasing I_p results in a lower ρ^*, affecting the LM penetration threshold, although the normalized intrinsic EF by B_t remain constant. Documenting the influence of plasma current on extrapolating this method to devices with high plasma current is crucial.
(3) Uncertainties persist regarding the nonlinear projection of this method for ITER's early operation. While simulations favor the method due to longer LM island growth time in H-mode electron density and temperature profiles, they also indicate potential challenges, such as requiring over 100% density rise, which may exceed the disruptive density limit. Additional simulations are warranted, particularly for ITER Ohmic plasmas.
(4) The effect of the resistive wall on island healing is not included in the MHD simulations, although it is known to inhibit the island from spinning up at low rotation frequencies [9, 53]. During the island healing process, once the RMP is turned off, the island remains locked to the intrinsic EF and gradually shrinks to a small width (less than 5%, as shown in figures 2(*e*) and 5(*d*)). It then spins up and quickly disappears, with the resistive wall effect acting to resist this spin-up. Given the much smaller island width and the short interaction time, we anticipate that omitting the resistive wall effect results in only a slight underestimation of the required density rise for achieving island healing.
(5) The effects of pellet injection on raising density in ITER, including pellet size, injection frequency, and speed, have not been considered in the simulations. Recent JET experiments [28] highlight the significance of these factors in achieving island healing. Thus, both experimental and simulation studies are essential to comprehensively document these factors and ensure the feasibility of the non-disruptive EF measurement method in ITER.

In conclusion, recent DIII-D experiments have demonstrated the viability of the non-disruptive EF measurement method with q_{95} as low as 3.2. Utilizing the TM1 code for nonlinear modeling, we successfully reproduce the experimental findings and elucidate the underlying mechanisms. Specifically, our simulations reveal that turning off RMP removes the drive for LM island and EM force on the island, and the concurrent density rise leads to increased plasma viscosity and stabilizes the LM island. Extending our simulations to explore the method's applicability in ITER's early operation reveals continued robustness for both $I_p = 5$ MA and 7.5 MA plasmas. Importantly, our findings underscore the advantage of swiftly implementing control actions to maximize effectiveness.

Acknowledgments

The author Q. Hu is grateful to Y. Gribov and L. Piron for providing detailed information on the EFCC power supplies in ITER. This material is based upon work supported by the US Department of Energy, Office of Science, Office of Fusion Energy Sciences, using the DIII-D National Fusion Facility, a DOE Office of Science user facility, under Award Nos. DE-AC02-09CH11466, DE-FC02-04ER54698, DE-FG02-04ER54761, and DE-SC0022270, the Technology Development Projects for Leading Nuclear Fusion through the National Research Foundation of Korea (NRF) funded by the Ministry of Science and ICT (No. RS-2024-00281276), and also by the New Faculty Startup Fund from Seoul National University. Q. Yu is partially supported by the Eurofusion Enabling Research Project (CfP-FSD-AWP24-ENR). His work has been carried out within the framework of the EUROfusion Consortium, funded by the European Union via the Euratom Research and Training Programme (Grant Agreement No. 101052200—EUROfusion). Views and opinions expressed are however those of the author(s) only and do not necessarily reflect those of the European Union or the European Commission. Neither the European Union nor the European Commission can be held responsible for them.

Disclaimer

ORCID iDs

Q.M. Hu https://orcid.org/0000-0002-8877-4988
N.C. Logan https://orcid.org/0000-0002-3268-7359
C. Paz-Soldan https://orcid.org/0000-0001-5069-4934
J. Barr https://orcid.org/0000-0001-7768-5931
S.K. Kim https://orcid.org/0000-0002-0701-8962
J. Hanson https://orcid.org/0000-0003-2432-4870
Y.Z. Jiang https://orcid.org/0000-0003-3252-8910
S.M. Yang https://orcid.org/0000-0003-1214-1268
A. Bortolon https://orcid.org/0000-0002-0094-0209
W. Choi https://orcid.org/0000-0002-6891-2300
Y.Q. Liu https://orcid.org/0000-0002-8192-8411
J.-K. Park https://orcid.org/0000-0003-2419-8667
E.J. Strait https://orcid.org/0000-0001-9215-3757
Q. Yu https://orcid.org/0000-0003-2722-4445

References

[1] Scoville J.T., Haye R.J.L., Kellman A.G., Osborne T.H., Stambaugh R.D., Strait E.J. and Taylor T.S. 1991 Locked modes in DIII-D and a method for prevention of the low density mode *Nucl. Fusion* **31** 875
[2] Hender T.C. *et al* 1992 Effect of resonant magnetic perturbations on COMPASS-C tokamak discharges *Nucl. Fusion* **32** 2091
[3] ITER Physics Expert Group on Disruptions, Plasma Control, and MHD and ITER Physics Basis Editors 1999 Chapter 3: MHD stability, operational limits and disruptions *Nucl. Fusion* **39** 2251
[4] Logan N.C. *et al* 2020 Empirical scaling of the n=2 error field penetration threshold in tokamaks *Nucl. Fusion* **60** 086010
[5] Park J.-K., Schaffer M.J., Haye R.J.L., Scoville T.J. and Menard J.E. 2011 Error field correction in DIII-D Ohmic plasmas with either handedness *Nucl. Fusion* **51** 023003
[6] Wang H. *et al* (EAST Contributors) 2018 Density scaling on n = 1 error field penetration in ohmically heated discharges in EAST *Nucl. Fusion* **58** 056024
[7] Wang H.-H. *et al* (EAST contributors) 2020 Toroidal field and q 95 scalings on error field penetration in EAST *Nucl. Fusion* **60** 126008
[8] La Haye R.J., Fitzpatrick R., Hender T.C., Morris A.W., Scoville J.T. and Todd T.N. 1992 Critical error fields for locked mode instability in tokamaks *Phys. Fluids* B **4** 2098
[9] Fitzpatrick R. 1993 Interaction of tearing modes with external structures in cylindrical geometry (plasma) *Nucl. Fusion* **33** 1049
[10] Buttery R.J. *et al* (JET Team, COMPASS-D Research Team, DIII-D Team) 1999 Error field mode studies on JET, COMPASS-D and DIII-D, and implications for ITER *Nucl. Fusion* **39** 1827
[11] Buttery R.J., Benedetti M.D., Hender T.C. and Tubbing B.J.D. 2000 Error field experiments in JET *Nucl. Fusion* **40** 807
[12] Finken K.H. *et al* 2005 Toroidal plasma rotation induced by the dynamic ergodic divertor in the TEXTOR tokamak *Phys. Rev. Lett.* **94** 015003
[13] Bock M.F.M.D., Classen I.G.J., Busch C., Jaspers R.J.E., Koslowski H.R. and Unterberg B. (TEXTOR Team) 2008 The interaction between plasma rotation, stochastic fields and tearing mode excitation by external perturbation fields *Nucl. Fusion* **48** 015007
[14] Wolfe S.M. *et al* 2005 Nonaxisymmetric field effects on Alcator C-Mod *Phys. Plasmas* **12** 056110
[15] Menard J.E. *et al* 2010 Progress in understanding error-field physics in NSTX spherical torus plasmas *Nucl. Fusion* **50** 045008
[16] Rao B., Ding Y.H., Yu K.X., Jin W., Hu Q.M., Yi B., Nan J.Y., Wang N.C., Zhang M. and Zhuang G. 2013 Measurement of 2/1 intrinsic error field of Joint TEXT tokamak *Rev. Sci. Instrum.* **84** 043504
[17] Paz-Soldan C., Buttery R.J., Garofalo A.M., Hanson J.M., Haye R.J.L., Lanctot M.J., Park J.K., Solomon W.M. and Strait E.J. 2014 The spectral basis of optimal error field correction on DIII-D *Nucl. Fusion* **54** 073013
[18] In Y., Park J.K., Jeon J.M., Kim J. and Okabayashi M. 2015 Extremely low intrinsic non-axisymmetric field in KSTAR and its implications *Nucl. Fusion* **55** 043004
[19] Wang H.-H. *et al* (The EAST Team) 2016 Observation of spectrum effect on the measurement of intrinsic error field on EAST *Nucl. Fusion* **56** 066011
[20] Strait E.J. *et al* 2014 Measurement of tokamak error fields using plasma response and its applicability to ITER *Nucl. Fusion* **54** 073004
[21] Shiraki D., Haye R.J.L., Logan N.C., Strait E.J. and Volpe F.A. 2014 Error field detection in DIII-D by magnetic steering of locked modes *Nucl. Fusion* **54** 033006
[22] Shiraki D., Paz-Soldan C., Hanson J.M., Haye R.J.L., Logan N.C., Olofsson K.E.J., Strait E.J., Sweeney R.M. and Volpe F.A. 2015 Measurements of the toroidal torque balance of error field penetration locked modes *Plasma Phys. Control. Fusion* **57** 025016
[23] Paz-Soldan C., Lanctot M.J., Logan N.C., Shiraki D., Buttery R.J., Hanson J.M., La Haye R.J., Park J.-K., Solomon W.M. and Strait E.J. 2014 The importance of matched poloidal spectra to error field correction in DIII-D *Phys. Plasmas* **21** 072503

[24] Lanctot M.J., Olofsson K.E.J., Capella M., Humphreys D.A., Eidietis N., Hanson J.M., Paz-Soldan C., Strait E.J. and Walker M.L. 2016 Error field optimization in DIII-D using extremum seeking control *Nucl. Fusion* **56** 076003
[25] Garofalo A.M., Haye R.J.L. and Scoville J.T. 2002 Analysis and correction of intrinsic non-axisymmetric magnetic fields in high-β DIII-D plasmas *Nucl. Fusion* **42** 1335
[26] Reimerdes H. *et al* 2009 Effect of resonant and non-resonant magnetic braking on error field tolerance in high beta plasmas *Nucl. Fusion* **49** 115001
[27] Paz-Soldan C., Hu Q., Logan N. and Park J.-K. 2022 Non-disruptive error field identification based on magnetic island healing *Nucl. Fusion* **62** 126007
[28] Piron L. *et al* (JET Contributors, the EUROfusion Tokamak Exploitation Team, the ASDEX Upgrade Team, MAST-U Team) 2024 Error field detection and correction studies towards ITER operation *Nucl. Fusion* **64** 066029
[29] Yu Q., Günter S. and Scott B.D. 2003 Numerical modeling of linear drift-tearing mode stability *Phys. Plasmas* **10** 797
[30] Yu Q. and Günter S. 2011 Plasma response to externally applied resonant magnetic perturbations *Nucl. Fusion* **51** 073030
[31] Hu Q.M., Nazikian R., Grierson B.A., Logan N.C., Paz-Soldan C. and Yu Q. 2020 The role of edge resonant magnetic perturbations in edge-localized-mode suppression and density pump-out in low-collisionality DIII-D plasmas *Nucl. Fusion* **60** 076001
[32] Groebner R.J. *et al* 2001 Progress in quantifying the edge physics of the H mode regime in DIII-D *Nucl. Fusion* **41** 1789
[33] Evans T.E. *et al* 2006 The physics of edge resonant magnetic perturbations in hot tokamak plasmas *Phys. Plasmas* **13** 056121
[34] Van Zeeland M.A., Boivin R.L., Carlstrom T.N., Deterly T. and Finkenthal D.K. 2006 Fiber optic two-color vibration compensated interferometer for plasma density measurements *Rev. Sci. Instrum.* **77** 10F325
[35] Hu Q., Du X., Yu Q., Logan N.C., Kolemen E., Nazikian R. and Jiang Z.H. 2019 Fast and pervasive heat transport induced by multiple locked modes in DIII-D *Nucl. Fusion* **59** 016005
[36] Du X.D. *et al* 2019 First observation of plasma healing via helical equilibrium in tokamak disruptions *Nucl. Fusion* **59** 094002
[37] Hu Q.M., Park J.-K., Yang S.M., Kim S.K., Logan N.C., Nazikian R., Kang J., Paz-Soldan C., Ko W.H. and Park G.Y. 2023 Validation of density pump-out by pedestal-foot magnetic island formation prior to ELM suppression in KSTAR and DIII-D tokamaks *Nucl. Fusion* **63** 096002
[38] Park J.-K. and Logan N.C. 2017 Self-consistent perturbed equilibrium with neoclassical toroidal torque in tokamaks *Phys. Plasmas* **24** 032505
[39] Yu Q., Günter S., Kikuchi Y. and Finken K.H. 2008 Numerical modelling of error field penetration *Nucl. Fusion* **48** 024007
[40] Hu Q., Logan N.C., Park J.-K., Paz-Soldan C., Nazikian R. and Yu Q. 2020 Nonlinear modeling of the scaling law for the m/n = 3/2 error field penetration threshold *Nucl. Fusion* **60** 076006
[41] Hu Q.M., Nazikian R., Grierson B.A., Logan N.C., Park J.-K., Paz-Soldan C. and Yu Q. 2019 The density dependence of edge-localized-mode suppression and pump-out by resonant magnetic perturbations in the DIII-D tokamak *Phys. Plasmas* **26** 120702
[42] Hu Q.M., Nazikian R., Grierson B.A., Logan N.C., Orlov D.M., Paz-Soldan C. and Yu Q. 2020 Wide operational windows of edge-localized mode suppression by resonant magnetic perturbations in the DIII-D tokamak *Phys. Rev. Lett.* **125** 045001
[43] Hu Q.M. *et al* 2021 Predicting operational windows of ELMs suppression by resonant magnetic perturbations in the DIII-D and KSTAR tokamaks *Phys. Plasmas* **28** 052505
[44] Grierson B.A. *et al* 2019 Main-ion intrinsic toroidal rotation across the ITG/TEM boundary in DIII-D discharges during ohmic and electron cyclotron heating *Phys. Plasmas* **26** 042304
[45] Breslau J., Gorelenkova M., Poli F., Sachdev J. and Yuan X. 2018 *TRANSP v18.2* (https://doi.org/10.11578/dc.20180627.4) (Computer Software)
[46] Hu Q., Rao B., Yu Q., Ding Y., Zhuang G., Jin W. and Hu X. 2013 Understanding the effect of resonant magnetic perturbations on tearing mode dynamics *Phys. Plasmas* **20** 092502
[47] Li L., Liu Y.Q., Loarte A., Pinches S.D., Polevoi A., Liang Y. and Zhong F.C. 2019 Modeling 3D plasma boundary corrugation and tailoring toroidal torque profiles with resonant magnetic perturbation fields in ITER *Nucl. Fusion* **59** 096038
[48] Loarte A. *et al* (the ITPA Scrape-off Layer and Divertor Physics Topical Group) 2007 Chapter 4: Power and particle control *Nucl. Fusion* **47** S203
[49] Hender T.C. *et al* (the ITPA MHD, Disruption and Magnetic Control Topical Group) 2007 Chapter 3: MHD stability, operational limits and disruptions *Nucl. Fusion* **47** S128
[50] Foussat A., Libeyre P., Mitchell N., Gribov Y., Jong C.T.J., Bessette D., Gallix R., Bauer P. and Sahu A. 2010 Overview of the ITER correction coils design *IEEE Trans. Appl. Supercond.* **20** 402–6
[51] Fitzpatrick R. 2012 Nonlinear error-field penetration in low density ohmically heated tokamak plasmas *Plasma Phys. Control. Fusion* **54** 094002
[52] Fitzpatrick R. 2022 Influence of anomalous perpendicular transport on linear tearing mode dynamics in tokamak plasmas *Phys. Plasmas* **29** 032507
[53] Pustovitov V.D. 2015 Energy principle for the modes interacting with a resistive wall in toroidal systems *Nucl. Fusion* **55** 033008